tvst

Glaucoma

Under Pressure: Lamina Cribrosa Pore Path Tortuosity in Response to Acute Pressure Modulation

Palaiologos Alexopoulos[1], Yoav Glidai[1], Zeinab Ghassabi[1], Bo Wang[2], Behnam Tayebi[1], Anse Vellappally[1], Mengfei Wu[1,3], Mengling Liu[1,3], Katie Lucy-Jones[1], Ronald Zambrano[1], Hiroshi Ishikawa[1], Joel S. Schuman[1,4–6], and Gadi Wollstein[1,4,6]

[1] Department of Ophthalmology, NYU Langone Health, New York University, New York, NY, USA
[2] UPMC Eye Center, Eye and Ear Institute, Ophthalmology and Visual Science Research Center, Department of Ophthalmology, University of Pittsburgh School of Medicine, Pittsburgh, PA, USA
[3] Division of Biostatistics, Departments of Population Health and Environmental Medicine, NYU Langone Health, New York University, New York, NY, USA
[4] Department of Biomedical Engineering, NYU Tandon School of Engineering, New York University, New York, NY, USA
[5] Department of Neuroscience and Physiology, NYU Langone Health, New York, NY, USA
[6] Center for Neural Science, New York University College of Arts and Sciences, New York, NY, USA

Correspondence: Gadi Wollstein, Department of Ophthalmology, NYU Langone Health, New York University, 222 East 41st Street, New York, NY 10017, USA. e-mail: gadi.wollstein@nyulangone.org

Received: September 28, 2022
Accepted: February 23, 2023
Published: April 5, 2023

Keywords: glaucoma; lamina cribrosa; optical coherence tomography

Citation: Alexopoulos P, Glidai Y, Ghassabi Z, Wang B, Tayebi B, Vellappally A, Wu M, Liu M, Lucy-Jones K, Zambrano R, Ishikawa H, Schuman JS, Wollstein G. Under pressure: Lamina cribrosa pore path tortuosity in response to acute pressure modulation. Transl Vis Sci Technol. 2023;12(4):4, https://doi.org/10.1167/tvst.12.4.4

Purpose: Lamina cribrosa (LC) deformation is hypothesized to play a major role in glaucoma pathogenesis. The purpose of this study was to determine in vivo how varying intraocular pressure (IOP) under fixed intracranial pressure (ICP), and vice versa, deforms the pore paths throughout the LC volume.

Methods: Spectral-domain optical coherence tomography scans of the optic nerve head were acquired from healthy adult rhesus monkeys under different pressures. IOP and ICP were controlled with gravity-based perfusion systems into the anterior chamber and lateral ventricle, respectively. IOP and ICP were modulated from baseline to high (19–30 mmHg) and highest (35–50 mmHg) levels while maintaining a fixed ICP of 8 to 12 mmHg and IOP of 15 mmHg, respectively. After three-dimensional registration and segmentation, the paths of pores visible in all settings were tracked based on their geometric centroids. Pore path tortuosity was defined as the measured distance divided by the minimal distance between the most anterior and posterior centroids.

Results: The median pore tortuosity at baseline varied among the eyes (range, 1.16–1.68). For the IOP effect under fixed ICP (six eyes, five animals), two eyes showed statistically significant increased tortuosity and one showed a decrease ($P < 0.05$, mixed-effects model). No significant change was detected in three eyes. When modulating ICP under fixed IOP (five eyes, four animals), a similar response pattern was detected.

Conclusions: Baseline pore tortuosity and the response to acute pressure increase vary substantially across eyes.

Translational Relevance: LC pore path tortuosity could be associated with glaucoma susceptibility.

Introduction

The lamina cribrosa (LC) is a meshwork of collagen fibers within the optic nerve head (ONH). The retinal ganglion cell (RGC) axons pass through the pores within this meshwork on their way to the brain. The LC provides structural and nutritional support to the RGC fibers as they pass through it.[1] Deformation of the LC is hypothesized to be a major cause of glaucomatous damage, as it is considered to be the biomechanically weakest region of the eye.[2–8] The LC is exposed to various forms of forces applied in different directions, such as the anterior–posterior force of the intraocular pressure (IOP), the posterior and circumferential force of the intracranial pressure (ICP), and

Copyright 2023 The Authors

This work is licensed under a Creative Commons Attribution-NonCommercial-NoDerivatives 4.0 International License.

Downloaded from intl.iovs.org on 04/26/2024

the blood pressure within the blood vessels exerting forces in varying directions.[9,10] In a previous in vivo study with healthy non-human primates, we demonstrated that acute modulation of IOP and ICP significantly alters the LC microstructure.[11]

The development of optical coherence tomography (OCT) has provided the opportunity to study the finer details of the LC in vivo.[12–17] Taking advantage of these developments, several studies have evaluated in vivo differences in LC macrostructure and microstructure between healthy and glaucoma eyes, as well as longitudinal changes that the LC undergoes as part of the glaucomatous process.[18–27] Because of the considerable postmortem changes the tissue undergoes, including the lack of blood pressure and collapse of the blood vessels, changes in fluid dynamics, and tissue stiffening, it is an important advantage to be able to evaluate those features in vivo. Furthermore, of upmost importance in understanding how forces and deformations of the LC actually affect the RGC axons is determining the pore path trajectory within the LC volume through which they pass. Because the axons themselves are not visible within the LC with OCT, tracing the pore path within the LC provides an indirect indicator of the path the axons undergo while passing through the lamina. A previous histology study has demonstrated that the vast majority of axons follow their LC pore path.[28] As the pore path tortuosity increases, the RGC axons passing through them experience axonal damage and blockage of axoplasmic flow, astrocyte and glial cell damage, and hypoperfusion with resulting ischemia to the optic nerve, all of which would contribute to glaucomatous neuropathy.[29] Most in vivo studies performed so far have been limited to examining the effect of pressure on the anterior surface of the lamina. Considering that the axons transverse the entire volume of the lamina, an analysis focusing on the anterior lamina only would be insufficient. In a recent publication, we demonstrated that microstructural deformation in response to pressure modulation occurs throughout the lamina volume and is not captured by anterior lamina analysis.[30] In this study, we evaluated the pore path through the entire LC volume.

The main hypothesis tested in this study was that increases in pressures will result in an increase in the tortuosity of pore paths. We also hypothesized that the magnitude of deformation and the effect of the pore path tortuosity would vary among eyes, reflecting the differences in biomechanical properties of the LC among eyes. The purpose of this study was to study in vivo the effects of IOP and ICP modulation on the pore path within the LC.

Methods

Healthy, adult rhesus macaque monkeys (*Macaca mulatta*) were used for this study. All procedures of this experiment were approved by the University of Pittsburgh's Institutional Animal Care and Use Committee and adhered to both the guidelines outlined in the National Institute of Health's Guide for the Care and Use of Laboratory Animals and the ARVO Statement for the Use of Animals in Ophthalmic and Vision Research. Prior to their participation in the current experiment, all animals were involved in other non-invasive or minimally invasive experiments that did not affect the eye, brain, or blood pressure. Animals were maintained in size-appropriate cages in a socialized and cognitive stimulation environment. Monkeys were given access to free water and a variety of enrichments, which included visual, audio, taste, and textures, in addition to encouraging the normal primate behaviors of grooming and foraging.

Experimental Design

The experimental design has been previously reported in detail.[11] Each animal was placed in a prone position on a surgical table with its head in an upright position, which allowed the scanning to take place. After injections of ketamine (20 mg/kg) and midazolam (0.25 mg/kg), the animals were intubated and mechanically ventilated with the administration of isoflurane (1%–3%) during the entirety of the procedure. Ocular movements were minimized by using vecuronium bromide (2 mg/hr) prior to image acquisition. During the entire duration of the experiment, each animal's vital signs (blood pressure, heart rate, oxygen saturation, temperature, and exhaled CO_2) were continuously monitored.

IOP and ICP were controlled via gravity-based perfusion systems that were connected into the anterior chamber of the eye and the lateral ventricle of the brain, respectively. For anterior chamber cannulation, a 27-gauge butterfly needle was used, and for the lateral ventricle a lumbar catheter (Medtronic, Dublin, Ireland) was used. The ICP was monitored by a fiberoptic pressure sensor inserted into the parenchyma of the brain (ICP EXPRESS Monitor; DePuy Synthes, Raynham, MA). At first, the ICP was maintained at baseline opening pressure (range, 8–12 mmHg), and the IOP was modulated to normal (15 mmHg), high (30 mmHg), and highest (40–50 mmHg) levels. In each pressure setting, an adjustment period of 5 minutes was employed to allow for the viscoelastic effects of the scleral canal and the optic nerve to dissipate.[31] After

Downloaded from intl.iovs.org on 04/26/2024

completing IOP modulation while maintaining a fixed ICP, the IOP was fixed at normal level (15 mmHg) while modulating ICP to the high (19–30 mmHg) and highest (35–45 mmHg) levels. These acute pressure modulation settings were selected to include both clinical and extreme levels to test maximal effect on the pore path. We also selected similar levels of IOP and ICP to allow comparison of their effects.

In each pressure setting, the LC was imaged using a spectral-domain OCT system (Leica, Wetzlar, Germany) with a scan rate of 20,000 a-scans/s and a broadband superluminescent diode light source (λ = 870 nm, $\Delta\lambda$ = 200 nm; Superlum, Dublin, Ireland). A 3.0 mm × 3.0 mm × 1.6-mm scan cube centered on the ONH was acquired with the enhanced depth imaging mode while focusing on the LC for maximum visibility of the entire LC depth. At least two scans were acquired in each pressure setting.

Image Analysis

The OCT scans were imported into ImageJ[32] (National Institutes of Health, Bethesda, MD) and adjusted to become isotropic in all three dimensions. The scans were contrast enhanced via the local contrast enhancement plugin (Contrast Limited Adaptive Histogram Equalization, or CLAHE) in ImageJ in order to optimize visualization, and the best scans were selected for the analysis by an experienced user while considering the visibility of the pores and beams and the presence of minimal motion artifacts. Scan selection was performed prior to any image analysis. The scans were straightened based on the line connecting the Bruch's membrane openings (BMO) in both horizontal and vertical cross-sectional views (b-scans) of the optic nerve. This was performed to obtain an accurate en face view of the LC in order to minimize artifacts caused by tilting when resampling the three-dimensional (3D) cube along the axial direction. Scans from each eye in the different pressure settings were registered manually in 3D based on structural landmarks. The region of the LC in which the pores and the beams were clearly identified was selected in each scan. Because there is marked localized variability in the lamina structure,[33] we used only the shared region between the varying pressure settings for each eye. Although this substantially reduced the size of the analyzable lamina, it prevented the possibility that changes detected were due to a different structure analyzed rather than actual structural changes. The surface visibility was defined as the overall projection of the analyzable area in each plane divided by the BMO area (Fig. 1). Within the shared analyzable lamina, the pores were automatically segmented using a previously described local thresholding segmentation algorithm.[34] The scan cubes were then sliced to a series of parallel single-pixel-thick en face slices from anterior to posterior aspect of the lamina.

The pore path was determined using a previously reported method.[35] In brief, the geometric centroid of each pore in each slice was detected, using a particle tracking algorithm in ImageJ (MTrack2). The maximum lateral shift of a pore centroid between consecutive slices was limited to 20 µm, which is smaller than a typical pore diameter. Centroids in consecutive planes were connected to form the pore path, and only paths longer than or equal to 60 µm were considered. The accuracy of the tracking algorithm was subjectively evaluated to rule out possible segmentation or tracking errors (Fig. 2). In the event of pore paths splitting into two separate paths or separate pores merging to form one pore, the paths were treated as new before and after the splitting or merging points. A MATLAB (The MathWorks, Natick, MA) code of our own design[36] was used to further analyze the pore paths. The tortuosity of each pore path was defined as the measured distance of the centroid path divided by the minimum distance between the first and last identified pore centroids (Fig. 3). The medians of all tortuosity values of identified pore paths in each pressure settings were reported. Tortuosity values close to 1 represent pores whose paths are nearly straight, whereas larger values represent tortuous pore paths in space.

Associations between baseline pore path tortuosity and ONH and lamina structure were evaluated using linear regression that included disc area (calculated as the area delineated by the BMO area), LC pore diameter (diameter of the largest sphere that fit within the segmented pores), beam thickness (diameter of the largest sphere that fit within the inverse of the segmented pores), ratio of beam thickness to pore diameter (BPR), mean pore area (confined within the segmented pores in every en face plane), and connective tissue volume fraction (CTVF), which was calculated as the total volume of the beams divided by the visible LC volume. We also examined the association between the length of each pore path and the shift of the pore centroid using the ONH geometric centroid as a reference point. The shift of a pore path was calculated by subtracting the distance between the centroid of the most anterior pore and the corresponding ONH centroid from the distance of the most posterior pore (Fig. 3). Positive values for the shift represent pore paths moving toward the ONH center, whereas negative values represent pore paths moving away from the ONH center. The association of tortuosity with the distance of the pores

Downloaded from intl.iovs.org on 04/26/2024

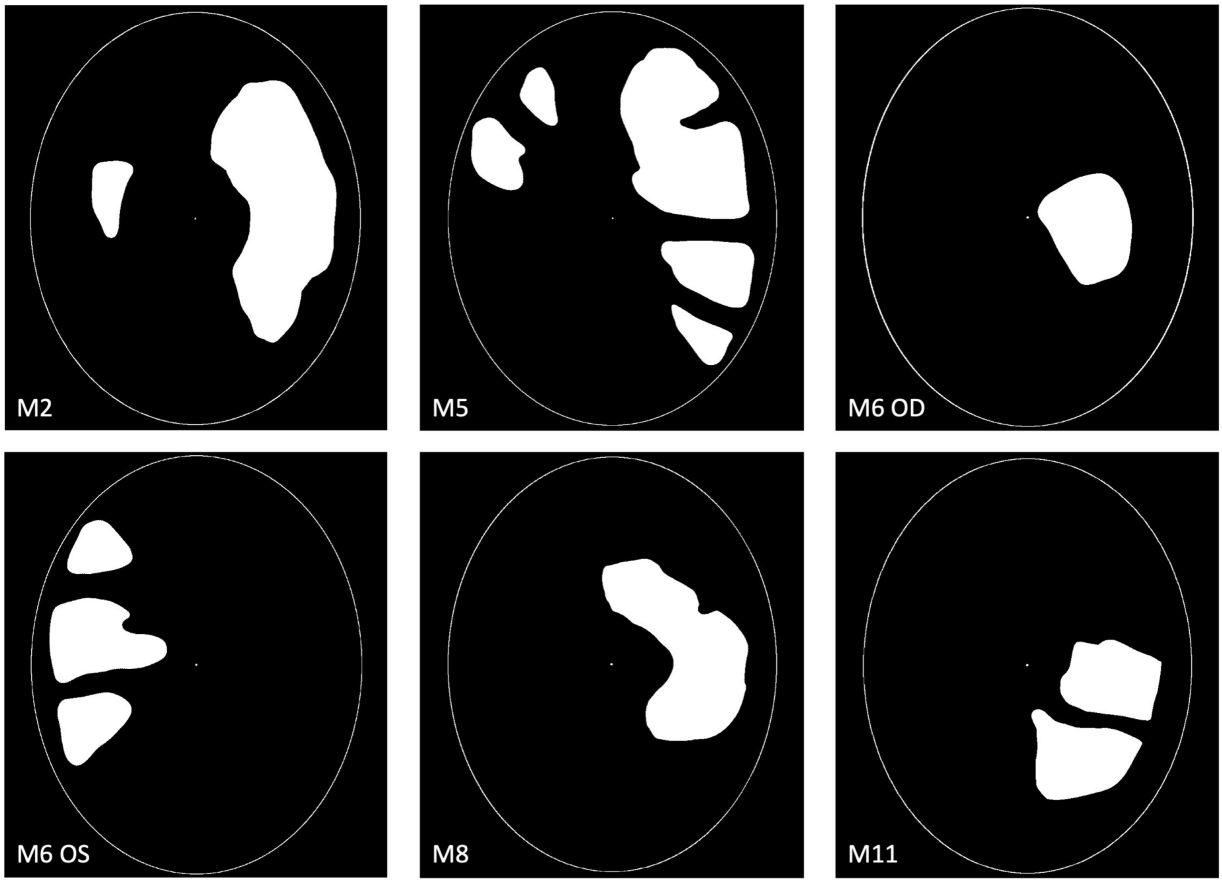

Figure 1. Projection of the visible LC area analyzed per eye.

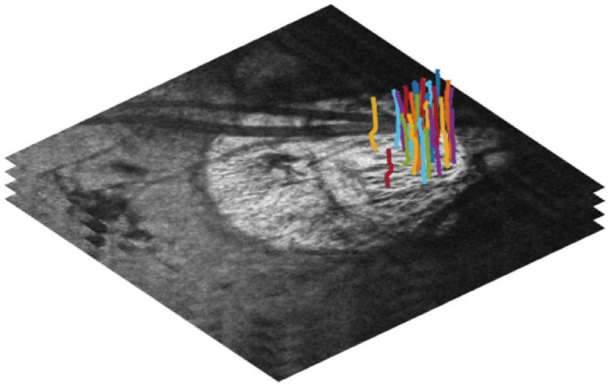

Figure 2. Tortuosity visualization.

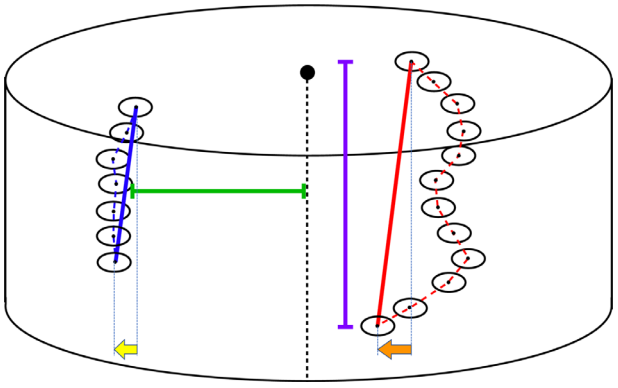

Figure 3. Example of pore paths and their tortuosity.

from the ONH centroid was studied to determine if the distance from the center affects the level of individual pore path tortuosity. Finally, an association was also investigated with the length of the pores to determine whether a longer pore path is more prone to tortuosity and vice versa, using repeated-measures correlation coefficients for each IOP and ICP setting (R Foundation for Statistical Computing, Vienna, Austria). $P < 0.05$ was considered statistically significant.

Results

Six eyes from five healthy adult rhesus macaque (age range, 7.9–14.4 years) were analyzed for the effect

translational vision science & technology

Downloaded from intl.iovs.org on 04/26/2024

Table 1. Demographics and Baseline LC Characteristics of Participating Animals

Animal ID	Laterality	Sex	Age (y)	Weight (kg)	BMO Area (mm^2)	Surface Visibility (%)	Mean Pore Area (μm^2)	Mean Beam Thickness (μm)	Mean Pore Diameter (μm)	BPR	CTVF (%)
M2	OD	F	14.4	7.2	1.82	21.3	813	38.64	23.63	1.64	76.1
M5	OD	M	8.7	8.9	2.29	26.4	1379	56.90	29.94	1.90	80.4
M6	OD	M	7.9	10.9	2.02	6.3	1035	47.05	36.47	1.78	78.3
M6	OS	M	7.9	10.9	2.13	12.7	1251	48.22	37.82	1.42	70.9
M8	OD	M	9.7	10.5	1.57	14.1	643	31.21	17.55	1.29	63.9
M11[a]	OD	M	8.7	12.2	1.40	12.1	736	28.32	19.93	1.28	65.7

[a]This eye was not used in the analysis of ICP modulation under fixed IOP.

Table 2. Pore Path Tortuosity Values for Each Eye Under Varying IOP Levels While Maintaining Fixed ICP of 8 to 12 mmHg

	Median (Lower Quartile, Upper Quartile)			
Animal ID	Baseline IOP	High IOP	Highest IOP	Pattern
M2 OD	1.16 (1.06, 1.23)	1.19 (1.06, 1.27))	1.21 (1.11, 1.27)[a]	↑
M5 OD	1.23 (1.10, 1.31)	1.25 (1.13, 1.31)	1.27 (1.14, 1.32)[a]	↑
M8 OD	1.30 (1.14, 1.38)	1.33 (1.17, 1.43)	1.35 (1.19, 1.48)	(–)
M11 OD	1.34 (1.18, 1.44)	1.37 (1.22, 1.48)	1.42 (1.17, 1.66)	(–)
M6 OD	1.35 (1.19, 1.42)	1.31 (1.28, 1.42)	1.36 (1.20, 1.41)	(–)
M6 OS	1.68 (1.30, 2.05)	1.45 (1.25, 1.52)[a]	1.51 (1.23, 1.65)[a]	↓

Pattern represents the overall change in pore path tortuosity in response to increase in IOP.
[a]Statistically significant ($P < 0.05$) as compared to baseline IOP.

of IOP under fixed, baseline ICP. For the analysis of the effect of ICP modulation under fixed IOP, one eye (M11 OD) was excluded due to missing data. The demographics of the animals and baseline characteristics of the LCs are summarized in Table 1, where marked variability in all parameters can be noted among the eyes. The surface visibility of analyzable LC in all pressure settings ranged between 6.3% and 26.4% of the LC volume across all eyes. No statistically significant association was detected between baseline tortuosity and any of the ONH or LC parameters.

IOP Modulation Under Fixed ICP

Using a linear quantile mixed-effects model of median tortuosity in each pressure setting while accounting for repeated measures, we detected two main patterns of pore path responses when IOP was increased while maintaining fixed ICP (Table 2). In the first pattern, noted in three eyes (M2, M5, and M6 OS), the pore paths statistically significantly changed (increased or decreased) with increasing IOP when compared with the baseline level. This "IOP deformers" pattern can be further divided into positive deformers (M2 and M5), where pore path tortuosity increased with increasing IOP, and a negative deformer (M6 OS), where tortuosity decreased with pressure increase. The second pattern, or the "non-IOP deformers," was noted in three eyes (M8, M11, and M6 OD), where no significant differences from baseline were detected in the pore path for any of the pressure settings. In general, the positive IOP deformer eyes had low baseline pore path tortuosity, and the negative deformer eyes had high baseline pore path tortuosity when compared with the non-deformer eyes. Assessing the distribution of the individual pore path tortuosity values for each eye demonstrated that, in the positive IOP deformers (Fig. 4, top panel, left and center plots), the majority of the pores displayed low tortuosity at baseline. In the presence of elevated IOP, this peak was reduced and there was a wide distribution toward higher tortuosity values. The negative IOP deformer (Fig. 4, top panel, right) shows the inverse pattern. In non-deformer eyes (Fig. 5, lower panel), there was no consistent pattern in the tortuosity distribution in the varying pressure settings. No statistically significant associations were

translational vision science & technology

Downloaded from intl.iovs.org on 04/26/2024

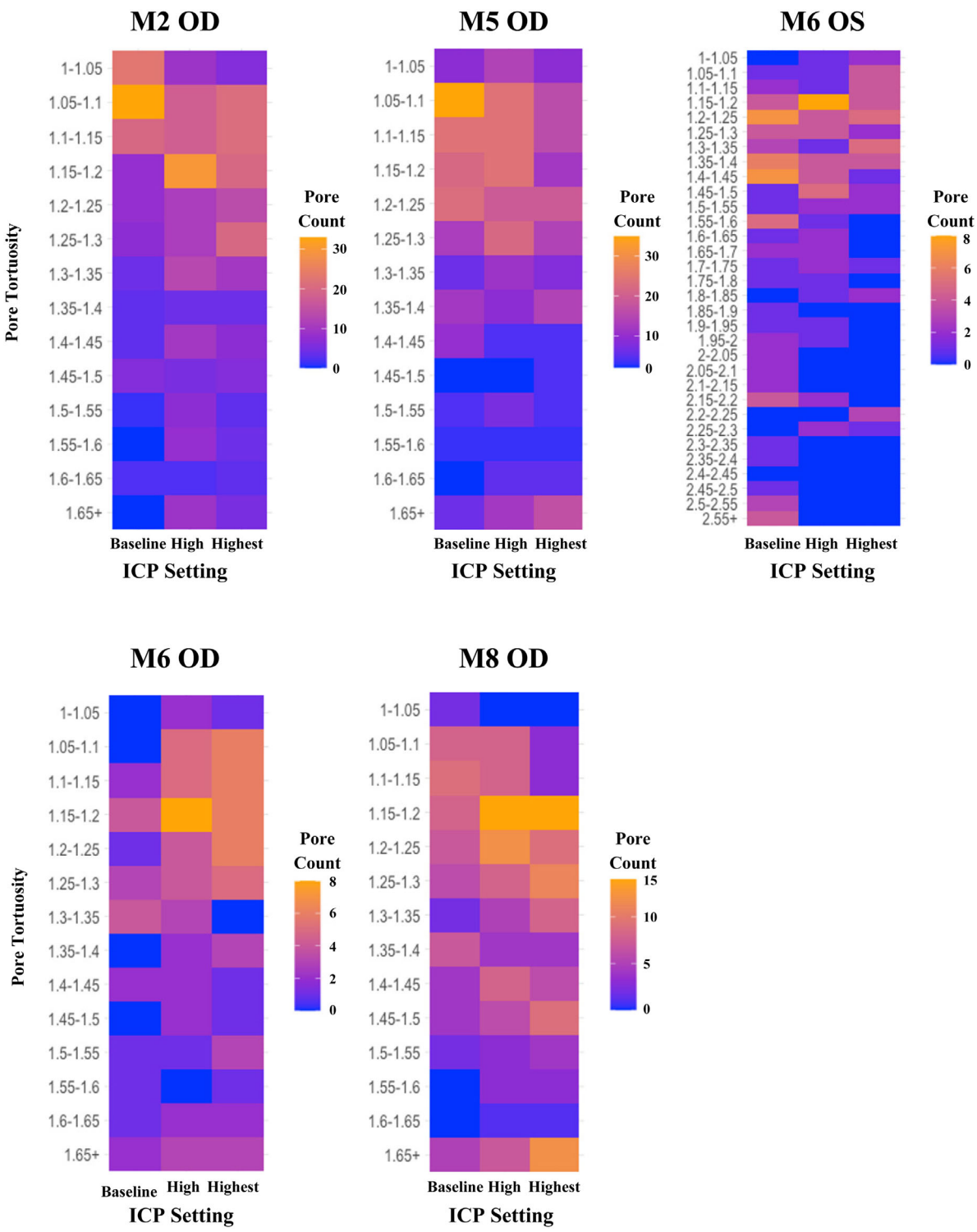

Figure 4. Heatmap plots of individual pore path tortuosity values of each eye at different IOP settings while maintaining fixed-baseline ICP.

detected between the pore paths tortuosity and the distance from the ONH center, the length of the pore paths, and the shift of the pore toward or away from the ONH center ($P > 0.05$).

ICP Modulation Under Fixed IOP

Changes in pore path tortuosity in response to modulating ICP in the presence of fixed IOP

Downloaded from intl.iovs.org on 04/26/2024

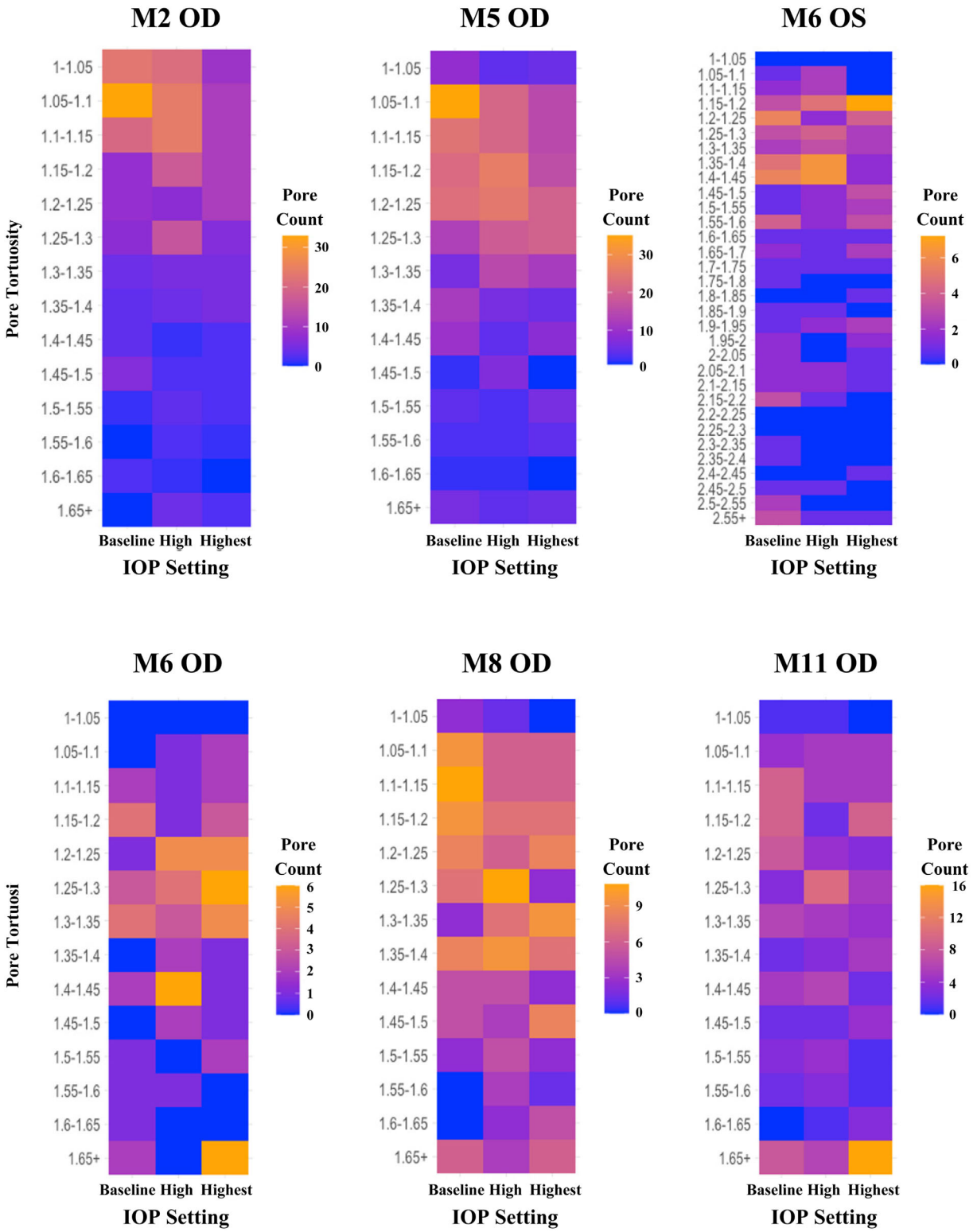

Figure 5. Heatmap plots of individual pore path tortuosity values of each eye at different ICP settings while maintaining fixed-baseline IOP.

translational vision science & technology

Downloaded from intl.iovs.org on 04/26/2024

Table 3. Pore Path Tortuosity Values for Each Eye Under Varying ICP Settings While Maintaining Fixed IOP of 15 mmHg

	Median (Lower Quartile, Upper Quartile)			
Animal ID	Baseline ICP	High ICP	Highest ICP	Pattern
M2 OD	1.16 (1.06, 1.23)	1.28 (1.12, 1.40)[a]	1.25 (1.12, 1.32)[a]	↑
M5 OD	1.23 (1.10, 1.31)	1.27 (1.12, 1.34)	1.31 (1.13, 1.40)[a]	↑
M8 OD	1.30 (1.14, 1.38)	1.31 (1.16, 1.43)	1.36 (1.19, 1.48)	(–)
M6 OD	1.35 (1.19, 1.42)	1.29 (1.15, 1.36)	1.29 (1.14, 1.41)	(–)
M6 OS	1.68 (1.30, 2.05)	1.47 (1.21, 1.63)[a]	1.37 (1.15, 1.42)[a]	↓

Pattern represents the overall change in pore path tortuosity in response to increase in ICP.
[a]Statistically significant ($P < 0.05$) as compared to baseline ICP.

(Table 3) were similar to those reported above for modulating IOP while maintaining fixed ICP. The same eyes that displayed pore path deformities with IOP were also susceptible to change with increasing ICP (M2, M5, and M6 OS). Furthermore, the positive IOP deformers (M2 and M5) were also positive ICP deformers, and the negative IOP deformer (M6 OS) was a negative ICP deformer. The two remaining IOP non-deformer eyes (M8 and M6 OD) did not show any significant change in tortuosity with increased ICP. The distributions of the individual pore path under varying ICP settings in the positive ICP deformers (M2 and M5) showed increased distribution toward higher tortuosity values in the presence of higher ICP (Fig. 5). The opposite pattern was noted for the negative ICP deformer eye (M6 OS). For the two ICP non-deformer eyes (M8 and M6 OD), an inconsistent pattern was noted.

A weak but positive significant association was detected between pore path tortuosity and distance of the pores from the ONH center when pooling data from all ICP setting ($r = 0.09$, $P < 0.001$). This association was stronger in the high and highest ICP levels when analyzed separately ($r = 0.12$ and 0.17, respectively; $P < 0.01$ in both). This association suggests that pore paths farther away from the ONH center (periphery) show increased tortuosity values associated with ICP modulation, whereas those closer to the center show less tortuosity values. To examine the possibility of scleral canal expansion affecting this finding, we repeated the analysis using the relative distance of each pore (ratio of distance of pore path from centroid divided by the distance of the ONH centroid to the edge of the nerve containing that pore centroid). The effect of canal expansion was minimal, and, in the vast majority, the relative distance was equal to the effect of the distance without adjustments. The tortuosity of the pores also displayed a significant association with the length of the pore paths when the data from all of the ICP settings were pooled ($r = 0.07$, $P < 0.01$); thus, longer pores tend to become more tortuous when exposed to increased level of ICP. No significant association was detected between path tortuosity and the shift of the pores toward or away from the nerve center for any ICP setting.

Discussion

Assessing the 3D LC pore path provides an indicator for the axonal path within the lamina. In this study, we evaluated in vivo changes in the lamina pore path in response to controlled IOP and ICP modulations. We detected large baseline variability in the pore path among eyes and in response to varying degree of IOP or ICP. The LC is a complex 3D structure with load-bearing beams of varying thickness, length, and orientation, as well as differing contents of collagen, elastin, and blood vessels. Therefore, the LC response to pressure modulation and the effect on the pore path are complicated. When IOP or ICP increases, the LC deformation and scleral canal expansion happen simultaneously. The lamina can deform posteriorly or anteriorly (pulled taut by scleral expansion), depending on whether compression or tension is the dominant force and/or the relative stiffness of the LC and sclera.

In our study, no significant association was detected between the baseline tortuosity and ONH and lamina parameters. This is likely due to the small sample size of our study. However, another potential conclusion is that pore path tortuosity cannot be predicted by the ONH structure but requires specific analyses examining the laminar microstructure only in baseline pressure without any modulations. Further investigation is warranted.

Two main patterns of pore path tortuosity in response to pressure modulations were detected in our healthy cohort: eyes with significant deformation

Downloaded from intl.iovs.org on 04/26/2024

(either increased or decreased tortuosity) and eyes with no significant deformation detected (Tables 2 and 3). The baseline LC microstructural parameters in our cohort (Table 1) are similar to those reported in a larger and independent cohort of healthy rhesus macaques, strengthening the generality of our findings.[37] Interestingly, we detected the same type of response per eye with either IOP or ICP challenges. The same patterns of response were detected in the same eyes when examining the LC microstructure in the entire LC depth in a previous study by our group.[30] This indicates that, within the pressure range used in this study, the inherent properties of the LC have a stronger impact on the response pattern than does orientation (anteroposterior vs. centripetal) of the inflicting force. We intentionally selected a pressure range that spanned from the clinical range (high IOP and ICP settings) to an exaggerated physiologic level (highest IOP and ICP) in order to capture the full range of tissue responses. The inherent structural and biomechanical variability of the LC across different eyes has been documented.[33,38] Nonetheless, our results indicate that eyes with baseline pore path tortuosity ranging between 1.30 and 1.35 do not deform significantly in either pressure settings or with IOP and ICP modulations. Although the tortuosity range in these eyes was narrow, there was a wide range in the BMO area, BPR, and CTVF, demonstrating the dissociation between the structure and its ability to deform. A stiffer LC or LC that is fully embedded within the scleral opening has limited ability to deform, and the initial pore path tortuosity will not change substantially even in the presence of an elevated pressure environment.

Although increased tortuosity in eyes with low initial pore path tortuosity in response to pressure elevation is intuitively understandable, a reduction in tortuosity with increased pressure is also plausible. Considering a theoretical situation where the anterior LC is constricted while the rest of the lamina freely expands would lead to high pore path tortuosity. When the IOP is elevated, the lamina is posteriorly displaced beyond the region of constriction, leading to tissue expansion and reduced pore path tortuosity. It is also plausible that increased IOP could have a more prominent effect on the scleral canal, such that canal expansion would cause the lamina to be pulled taut, leading to no significant change in pore paths. Our study was not designed to elucidate these potential explanations, and further investigation is warranted. Shifting of the lamina pores in response to in vivo pressure modulation has been previously reported.[39] However, this study evaluated only the anterior surface of the LC and did not consider the full 3D structure of the lamina. An increase in pore path tortuosity could contribute to axonal damage and blockage of axoplasmic flow at the level of the LC, astrocyte and glial cell damage, and hypoperfusion with resulting ischemia to the optic nerve, all of which would contribute to glaucomatous neuropathy.

A previous study has reported higher tortuosity in glaucomatous and glaucoma suspect human eyes when compared to healthy individuals.[36] The clinical implications of the varying patterns of response we report and their association with the risk of developing glaucoma or having a more aggressive disease should be further evaluated in longitudinal studies.

The association displayed between individual pore path tortuosity and the distance from the ONH center for the high and highest ICP settings can be explained by the nature of the stress applied to the LC. The ICP is a multidirectional force from the subarachnoid space that primarily affects the LC posteriorly and circumferentially; therefore, it is an expected finding that pores located farther away from the ONH center would be primarily affected compared with pores closer to it. In contrast, the IOP acts mainly on the anterior surface of the lamina and parallel to the path of the pores, which could explain why no association was found between the tortuosity and the distances in the increasing IOP settings. It should be noted that our study was not designed to examine the effect of altered IOP and ICP on the ONH size, and further investigation is warranted.

Some limitations of this study should be considered. The sample size of our study was small for obvious humane reasons, thus limiting the ability to draw rigid conclusions about the changes in tortuosity of the pores. Nevertheless, even with this small sample size, we were able to meet significance levels for several analyses, highlighting the statistical strength of these findings. Another limitation is the limited visibility of the LC which is an inevitable constraint of the technology. This is enhanced by the fact that, in order to ensure the reliability of our analysis, only the shared regions of the lamina across multiple IOP and ICP settings were analyzed to examine the same structures across all scans; therefore, poor visibility in a single pressure setting for a given eye limited the analyzable lamina across all scans. Subsequently, we could not analyze the entire volume of the LC in each eye but rather focused on changes detected on visible pore paths. Nevertheless, considering the large inter-eye variability in structure and in response to pressure modulation, analysis per eye is the most appropriate approach. Finally, because this study addressed only acute changes in healthy primate eyes, responses in glaucomatous eyes require further investigation.

Downloaded from intl.iovs.org on 04/26/2024

In conclusion, we have shown that pore path tortuosity varies among eyes in response to acute modulation of IOP and ICP in healthy nonhuman primates. The clinical implication of the different response patterns requires further longitudinal investigation.

Acknowledgments

Supported by grants from the National Eye Institute, National Institutes of Health (R01-EY030770, R01-EY025011, R01-EY013178, P30-EY013079); by an unrestricted grant from Research to Prevent Blindness; and by the Lighthouse Guild.

Disclosure: **P. Alexopoulos**, None; **Y. Glidai**, None; **Z. Ghassabi**, None; **B. Wang**, None; **B. Tayebi**, None; **A. Vellappally**, None; **M. Wu**, None; **M. Liu**, None; **K. Lucy-Jones**, None; **R. Zambrano**, None; **H. Ishikawa**, None; **J.S. Schuman**, Zeiss (R); **G. Wollstein**, None

References

1. Elkington AR, Inman CB, Steart PV, Weller RO. The structure of the lamina cribrosa of the human eye: An immunocytochemical and electron microscopical study. *Eye (Lond)*. 1990;4(pt 1):42–57.
2. Downs JC, Girkin CA. Lamina cribrosa in glaucoma. *Curr Opin Ophthalmol*. 2017;28(2):113–119.
3. Wilczek M. The lamina cribrosa and its nature. *Br J Ophthalmol*. 1947;31(9):551–565.
4. Lee SH, Kim TW, Lee EJ, Girard MJ, Mari JM. Diagnostic power of lamina cribrosa depth and curvature in glaucoma. *Invest Ophthalmol Vis Sci*. 2017;58(2):755–762.
5. Wang X, Tun TA, Nongpiur ME, et al. Peripapillary sclera exhibits a v-shaped configuration that is more pronounced in glaucoma eyes. *Br J Ophthalmol*. 2022;106(4):491–496.
6. Andrade JCF, Kanadani FN, Furlanetto RL, Lopes FS, Ritch R, Prata TS. Elucidation of the role of the lamina cribrosa in glaucoma using optical coherence tomography. *Surv Ophthalmol*. 2022;67(1):197–216.
7. Hollander H, Makarov F, Stefani FH, Stone J. Evidence of constriction of optic nerve axons at the lamina cribrosa in the normotensive eye in humans and other mammals. *Ophthalmic Res*. 1995;27(5):296–309.
8. Quigley HA, Addicks EM, Green WR, Maumenee AE. Optic nerve damage in human glaucoma. II. The site of injury and susceptibility to damage. *Arch Ophthalmol*. 1981;99(4):635–649.
9. Sigal IA, Yang H, Roberts MD, et al. IOP-induced lamina cribrosa deformation and scleral canal expansion: Independent or related? *Invest Ophthalmol Vis Sci*. 2011;52(12):9023–9032.
10. Grytz R, Fazio MA, Libertiaux V, et al. Age- and race-related differences in human scleral material properties. *Invest Ophthalmol Vis Sci*. 2014;55(12):8163–8172.
11. Wang B, Tran H, Smith MA, et al. In-vivo effects of intraocular and intracranial pressures on the lamina cribrosa microstructure. *PLoS One*. 2017;12(11):e0188302.
12. Furlanetto RL, Park SC, Damle UJ, et al. Posterior displacement of the lamina cribrosa in glaucoma: In vivo interindividual and intereye comparisons. *Invest Ophthalmol Vis Sci*. 2013;54(7):4836–4842.
13. Park SC, De Moraes CG, Teng CC, Tello C, Liebmann JM, Ritch R. Enhanced depth imaging optical coherence tomography of deep optic nerve complex structures in glaucoma. *Ophthalmology*. 2012;119(1):3–9.
14. Park HY, Park CK. Diagnostic capability of lamina cribrosa thickness by enhanced depth imaging and factors affecting thickness in patients with glaucoma. *Ophthalmology*. 2013;120(4):745–752.
15. Park HY, Jeon SH, Park CK. Enhanced depth imaging detects lamina cribrosa thickness differences in normal tension glaucoma and primary open-angle glaucoma. *Ophthalmology*. 2012;119(1):10–20.
16. Tan NY, Koh V, Girard MJ, Cheng CY. Imaging of the lamina cribrosa and its role in glaucoma: A review. *Clin Exp Ophthalmol*. 2018;46(2):177–188.
17. Lee EJ, Kim TW, Kim M, Kim H. Influence of lamina cribrosa thickness and depth on the rate of progressive retinal nerve fiber layer thinning. *Ophthalmology*. 2015;122(4):721–729.
18. Ren R, Yang H, Gardiner SK, et al. Anterior lamina cribrosa surface depth, age, and visual field sensitivity in the Portland Progression Project. *Invest Ophthalmol Vis Sci*. 2014;55(3):1531–1539.
19. Ing E, Ivers KM, Yang H, et al. Cupping in the monkey optic nerve transection model consists of prelaminar tissue thinning in the absence of posterior laminar deformation. *Invest Ophthalmol Vis Sci*. 2016;57(6):2914–2927.
20. Yang H, Qi J, Hardin C, et al. Spectral-domain optical coherence tomography enhanced depth imaging of the normal and glaucomatous nonhuman primate optic nerve head. *Invest Ophthalmol Vis Sci*. 2012;53(1):394–405.

Downloaded from intl.iovs.org on 04/26/2024

21. Ivers KM, Yang H, Gardiner SK, et al. In vivo detection of laminar and peripapillary scleral hypercompliance in early monkey experimental glaucoma. *Invest Ophthalmol Vis Sci*. 2016;57(9):OCT388–OCT403.
22. Yang H, He L, Gardiner SK, et al. Age-related differences in longitudinal structural change by spectral-domain optical coherence tomography in early experimental glaucoma. *Invest Ophthalmol Vis Sci*. 2014;55(10):6409–6420.
23. Luo H, Yang H, Gardiner SK, et al. Factors influencing central lamina cribrosa depth: A multicenter study. *Invest Ophthalmol Vis Sci*. 2018;59(6):2357–2370.
24. Strouthidis NG, Fortune B, Yang H, Sigal IA, Burgoyne CF. Longitudinal change detected by spectral domain optical coherence tomography in the optic nerve head and peripapillary retina in experimental glaucoma. *Invest Ophthalmol Vis Sci*. 2011;52(3):1206–1219.
25. Strouthidis NG, Fortune B, Yang H, Sigal IA, Burgoyne CF. Effect of acute intraocular pressure elevation on the monkey optic nerve head as detected by spectral domain optical coherence tomography. *Invest Ophthalmol Vis Sci*. 2011;52(13):9431–9437.
26. Li F, Yang Y, Sun X, et al. Digital gonioscopy based on three-dimensional anterior-segment OCT: An international multicenter study. *Ophthalmology*. 2022;129(1):45–53.
27. Wang B, Nevins JE, Nadler Z, et al. In vivo lamina cribrosa micro-architecture in healthy and glaucomatous eyes as assessed by optical coherence tomography. *Invest Ophthalmol Vis Sci*. 2013;54(13):8270–8274.
28. Morgan JE, Jeffery G, Foss AJ. Axon deviation in the human lamina cribrosa. *Br J Ophthalmol*. 1998;82(6):680–683.
29. Stowell C, Burgoyne CF, Tamm ER, Ethier CR. Biomechanical aspects of axonal damage in glaucoma: A brief review. *Exp Eye Res*. 2017;157:13–19.
30. Glidai Y, Lucy KA, Schuman JS, et al. Microstructural deformations within the depth of the lamina cribrosa in response to acute in vivo intraocular pressure modulation. *Invest Ophthalmol Vis Sci*. 2022;63(5):25.
31. Downs JC, Suh JK, Thomas KA, Bellezza AJ, Hart RT, Burgoyne CF. Viscoelastic material properties of the peripapillary sclera in normal and early-glaucoma monkey eyes. *Invest Ophthalmol Vis Sci*. 2005;46(2):540–546.
32. Schindelin J, Arganda-Carreras I, Frise E, et al. Fiji: An open-source platform for biological-image analysis. *Nat Methods*. 2012;9(7):676–682.
33. Ivers KM, Sredar N, Patel NB, et al. In vivo changes in lamina cribrosa microarchitecture and optic nerve head structure in early experimental glaucoma. *PLoS One*. 2015;10(7):e0134223.
34. Nadler Z, Wang B, Wollstein G, et al. Automated lamina cribrosa microstructural segmentation in optical coherence tomography scans of healthy and glaucomatous eyes. *Biomed Opt Express*. 2013;4(11):2596–2608.
35. Wang B, Lucy KA, Schuman JS, et al. Tortuous pore path through the glaucomatous lamina cribrosa. *Sci Rep*. 2018;8(1):7281.
36. Wang B, Lucy KA, Schuman JS, et al. Tortuous pore path through the glaucomatous lamina cribrosa. *Sci Rep*. 2018;8(1):7281.
37. Sainulabdeen A, Glidai Y, Wu M, et al. 3D microstructure of the healthy non-human primate lamina cribrosa by optical coherence tomography imaging. *Transl Vis Sci Technol*. 2022;11(4):15.
38. Jonas JB, Kutscher JN, Panda-Jonas S, Hayreh SS. Lamina cribrosa thickness correlated with posterior scleral thickness and axial length in monkeys. *Acta Ophthalmol*. 2016;94(8):e693–e696.
39. Wang YX, Zhang Q, Yang H, Chen JD, Wang N, Jonas JB. Lamina cribrosa pore movement during acute intraocular pressure rise. *Br J Ophthalmol*. 2020;104(6):800–806.

Downloaded from intl.iovs.org on 04/26/2024